PHYSICAL REVIEW A **69**, 042708 (2004)

Beam-loss spectroscopy of cold collisions in a bright sodium beam

Jaime Ramirez-Serrano,* W. DeGraffenreid,† and John Weiner‡
Laboratory of Atomic, Molecular, and Optical Science and Engineering, University of Maryland, College Park, Maryland 20742, USA

Eite Tiesinga and P. S. Julienne
Atomic Physics Division, National Institute of Standards and Technology, 100 Bureau Drive, Stop 8423,
Gaithersburg, Maryland 20899-8423, USA

(Received 8 November 2003; published 9 April 2004)

We report beam-loss photoassociation (PA) spectra of cold collisions within a slow, bright Na atom beam near the D_1 resonance line. The high collimation and brilliance of the atomic beam permits the detection of atomic fluorescence loss resulting from the photoassociation of cold sodium atoms. The results show that even at high PA laser intensities, where strong coupling of the colliding atoms to the optical field might obscure spectral features, vibrational and rotational progressions are surprisingly well resolved. We attribute the conservation of narrow spectral features to the properties of the saturated line shapes and to the unconventional collision energy distribution in one-dimensional (1D) single-beam collisions compared to 3D collisions in a gas cell.

DOI: 10.1103/PhysRevA.69.042708 PACS number(s): 34.50.Rk, 32.80.Pj, 33.80.Ps

I. INTRODUCTION

Since the first observation of cold collisions in samples of optically cooled and confined atoms in a dipole trap by Gould *et al.* [1] magneto-optical traps (MOTs) have provided the main environment to investigate the physics of cold collisions [2–5]. The observation of cold collisions is typically carried out by monitoring the ions produced during a photoassociative ionization (PAI) process or by observing the loss of atom fluorescence resulting from collisional photoassociation (PA) into excited-state molecules. In conventional three-dimensional atom traps, however, spatial averaging of molecular collision axes with respect to any space-fixed direction obscures alignment and orientation effects that may be inherent in the collision process. Even in conventional thermal atomic beams measurement of alignment and orientation effects is very difficult to carry out due to low density and high atom beam divergence. In a highly collimated (briliant) and translationally cold atom beam, however, DeGraffenreid *et al.* [6] and Ramirez-Serrano *et al.* [7] demonstrated alignment and orientation effects in the sodium PAI spectrum by detecting and measuring the molecular $\mathrm{Na_2}^+$ ions produced as a function of detuning and polarization of the PA laser with respect to the collision axis.

We report here the use of a brilliant atom beam with a density comparable to that obtained in conventional bright MOTs of $(1\pm0.5)\times10^{10}\ \mathrm{cm}^{-3}$ to study fluorescence loss or "beam-loss" spectra (as opposed to "trap-loss" spectra in MOTs) of cold Na atoms near the D_1 transition line. The spectra are obtained by monitoring the loss of fluorescence in the atomic beam induced by a high-intensity PA laser as it scans the photoassociation transitions to the red of the D_1 line. Fluorescence loss is detected using a weak laser probe beam located a short distance downstream from the PA zone and tuned to the atomic resonance line. The fluorescence signal excited by the probe laser is recorded as a function of the PA laser detuning from the $3\,^2S_{1/2}(f=2)\rightarrow3\,^2P_{1/2}(f=2)$ transition line.

In the final section of the paper we will adapt the usual theory of photoassociation line shapes to the high-intensity regime of these experiments. Although the theory is much more approximate and qualitative than is possible for low-intensity experiments, it does give an account of the surprising robustness of the relatively narrow experimental photoassociation features, clearly resistant to strong power broadening. The narrowness arises from collision energies contributing small stimulated emission widths. These contributions are enhanced by the quasi-one-dimensional geometry of the atom beam.

II. EXPERIMENTAL APPARATUS

The experiments are carried out using the atomic beam system described in detail in Refs. [7,8] and shown in Fig. 1. The atomic beam characteristics obtained using this system are summarized in Table I. The intrabeam, longitudinal collision temperature is 4 mK [7,8].

To detect the beam-loss spectra induced by the PA laser, a weak probe beam, with an intensity of $5.0\ \mathrm{mW\ cm}^{-2}$, interacts with the atomic beam a short distance downstream from the PA zone (see Fig. 2). The fluorescence intensity is monitored by a photomultiplier tube below the probe zone. Scattered light from the two-dimensional (2D) MOT and postcollimation regions just 20 mm upstream interfere with the fluorescence measurements. To reduce these effects, a series of small apertures leading to the photomultiplier tube are

---

[*] Present address: Jet Propulsion Laboratory, Quantum Sciences Group, 4800 Oak Grove Drive, MS 298-100, Pasadena, CA 91109.

[†] Present address: Department of Physics and Astronomy, California State University, Sacramento, CA 95819-6041.

[‡] Present address: Université Paul Sabatier, IRSAMC-LCAR, 118 route de Narbonne, 31062 Toulouse, France.

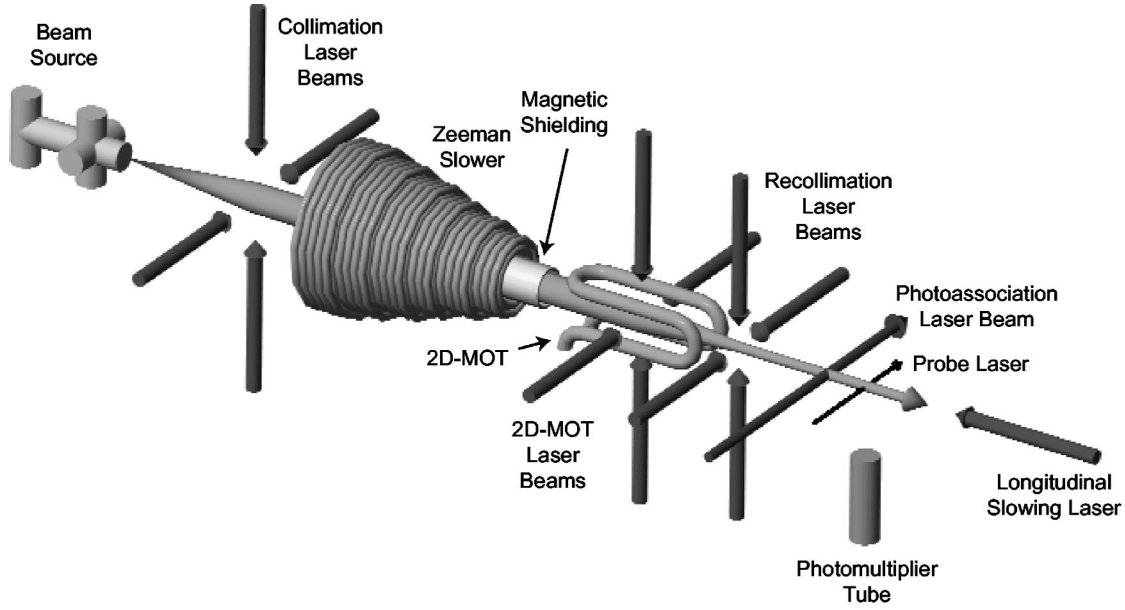

FIG. 1. Schematic of bright-beam apparatus with principal components labeled. See Refs. [7,8] for a full description.

adjusted to minimize scattered light coming from anywhere except the probe zone.

As the PA laser forms molecules, it reduces the atom number, creating dips in the fluorescence spectrum. To optimize the sensitivity of the fluorescence measurements to the PA beam-loss signal, different geometrical parameters must be considered. As is evident from Fig. 2, if the beam-loss probe beam covers only partially the zone of decreased atom density, the photoassociation signal cannot be detected with maximum efficiency. Obtaining an acceptable beam-loss signal requires that the probe beam diameter match that of the PA laser and that the PA and probe zone be carefully aligned along the longitudinal atom beam axis.

At low PA laser power we were not able to measure an acceptable beam-loss spectrum. We attribute this failure to PA and probe laser misalignment together with the lower rate of photoassociation at low PA laser intensity. To increase the PA laser intensity, while at the same time not decreasing the residence of the atoms inside the PA zone, the PA laser was focused by a combination of cylindrical and spherical lenses to a line 50 μm wide and 1 mm long along the centerline of the atomic beam. The resulting laser intensity of 600 W cm^{-2} provides an acceptable beam-loss signal and signal-to-noise ratio. A similar setup is used to focus the probe beam to comparable size characteristics as the PA laser, however, the intensity is maintained below saturation at 5.0 mW cm^{-2}.

Another factor to consider is the residual transverse velocity of about 25 cm s^{-1} that the atoms have after passing through the last optical molasses stage. Atoms unaffected by the PA laser eventually drift transversely into the fluorescence hole opened in the photoassociation zone, thereby decreasing the signal-to-background ratio of the fluorescence-

TABLE I. Summary of beam characteristics. The observed velocity distributions are to good approximation Gaussian parametrized by $\exp[-4(v-v_s)^2/(\Delta v_s)^2]$, where the subscript s is either $\perp$ or $\parallel$. The mean velocity $v_\perp$ along the transverse direction is chosen to be zero. One-standard-deviation uncertainties are quoted.

n	Density (atoms/cm^3)	$(1\pm0.5)\times10^{10}$
$v_\parallel$	Longitudinal velocity (m/s)	350 ± 5
$\Delta v_\parallel$	Longitudinal velocity spread (m/s)	5 ± 1
$\Delta v_\perp$	Transverse velocity spread (m/s)	0.25 ± 0.1
Ω	Solid angle (sr)	$(2\pm1)\times10^{-6}$
Δr	Beam radius in PA/probe zone (cm)	0.03 ± 0.01

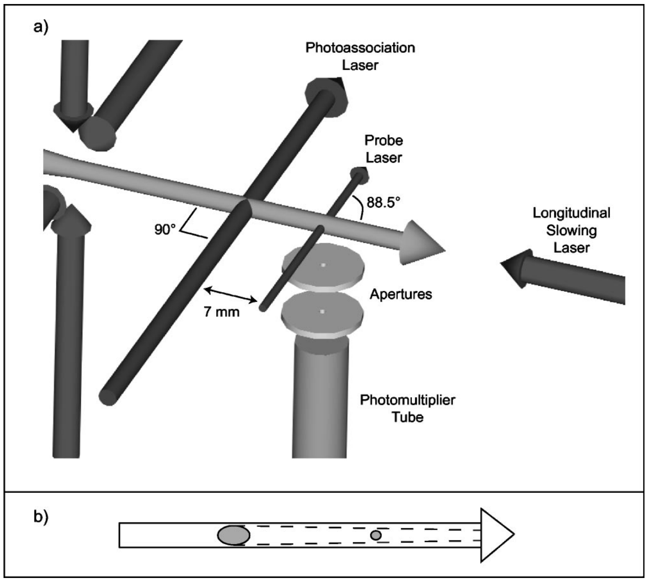

FIG. 2. (a) Detail of the experimental setup of the beam-loss spectroscopy system showing the relative disposition of the PA laser, the probe laser, and the fluorescence detector. (b) Schematic of the geometry of the fluorescence depletion at the PA laser spot (left spot) and subsequent atom depletion channel cut into the beam downstream. The small spot to the right indicates the position of the probe beam.

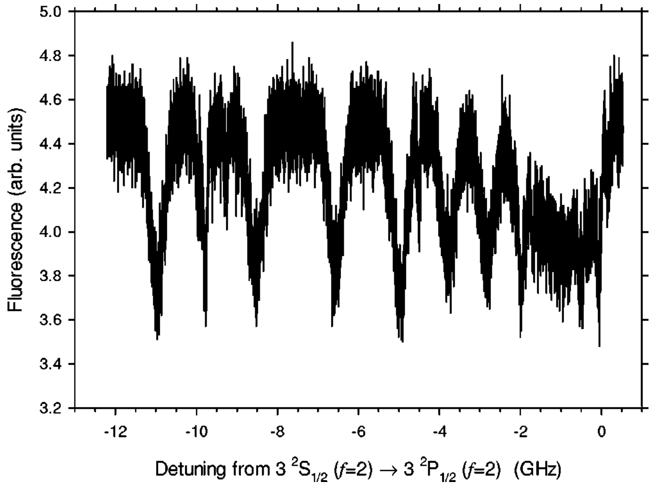

FIG. 3. Beam-loss spectrum for PA laser polarization parallel to the atom beam over the range of measurements from to −12 GHz to 0 GHz detuning to the red of the $^2S_{1/2}(f=2)+{}^2P_{1/2}(f=2)$ dissociation limit for an atomic beam without spin polarization. An assignment of the spectral structure is discussed in Sec. III C

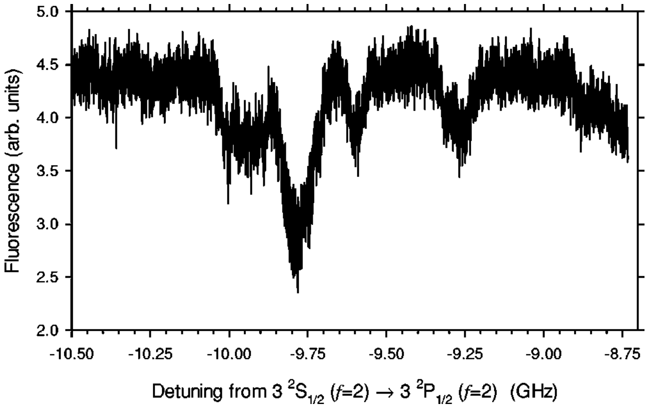

FIG. 4. Beam-loss spectrum for PA light polarization parallel to the atom beam close to the dip occurring at $\simeq -10$ GHz detuning to the red of the $^2S_{1/2}(f=2)+{}^2P_{1/2}(f=2)$ dissociation limit. The atom ground-state populations have not been spin polarized. The fluorescence-loss dips appear to be part of a rotational progression, and an assignment of the spectral features is discussed in Secs. III B and III C.

loss measurements. This loss is proportional to the downstream distance traveled from PA zone to detection zone. Under our current experimental conditions it takes more than 50 cm of longitudinal distance to close the fluorescence hole. Hence, this factor is not very important during the present experiments, but would become increasingly significant for longitudinally slower atomic beams.

III. BEAM-LOSS SPECTRA

To obtain the beam-loss spectra we use a similar procedure to that of Ramirez-Serrano *et al.* [7]. The PA laser intersects the atom beam at right angles a few centimeters downstream from the atomic beam extruder described elsewhere [7,8]. To obtain the beam-loss spectrum as a function of laser detuning, the PA laser frequency was scanned to the red of the $3\,^2S_{1/2}(f=2)\rightarrow 3\,^2P_{1/2}(f=2)$ atomic sodium line over a range of 12 GHz. The procedure was repeated for each of the three polarization cases of the PA laser: linear polarization parallel and perpendicular to the atom beam as well as circular polarization. In all cases the light propagation direction was maintained orthogonal to the atom beam. The PA laser was first calibrated to a known frequency by using the absorption signal from an iodine cell, together with a feature from the saturation absorption spectrum of sodium.

A beam-loss spectrum for the case of atom ground-state populations of the $3\,^2S_{1/2}(f=2)$ level (without spin polarization), covering the range from −12 GHz to 0 GHz, is shown in Fig. 3. There appears to be one feature and one progression: the feature near −10 GHz detuning corresponds to a relatively narrow transition (∼100 MHz) and the progression, comprising six or seven peaks, exhibits somewhat wider transitions (∼500 MHz). Initially it may seem surprising that these well-defined spectral features resist power broadening in the presence of a very intense light field. At a PA laser intensity of 600 W cm^{-2} the photoassociation process takes place in a strong-field regime. The stimulated transition rate between the ground-state collision channel and the 0_g^- excited state, for example, has a nominal order of magnitude [10,11] of $\approx 1-10$ GHz which is comparable to the spacing between the vibrational levels. The weak-field molecular potentials should be strongly perturbed, and one would expect the positions and widths of the vibrational progressions to be shifted and broadened into the background. Nevertheless, we can assign tentatively the unexpectedly narrow feature (∼100 MHz) to the 0_g^- excited potential. The progression associated with the wider lines (∼500 MHz) could be due to the 1_g or 0_u^+ potential curves dissociating to the $3\,^2S_{1/2}+3\,^2P_{1/2}$ atom pair limit (see potential curves in Fig. 7). A theoretical analysis of the spectrum will be presented in Sec. III C that accounts for the robustness to power broadening.

A. Spectra for different polarizations

By amplifying the detuning scale in Fig. 3 it is possible to see rotational structure associated with some of the tentatively identified 0_g^- dips. For the dip occurring at $\simeq -10$ GHz a more detailed scan, only 2 GHz wide, is shown in Fig. 4 for the case of PA laser polarization parallel to the atom beam axis. The population of the $f=2$ hyperfine sublevels of the participating atoms was left unpolarized. Two spectra similar to those of Fig. 4 are shown in Fig. 5 to contrast the effect of atom spin polarization on the rotational progression. The top spectrum shows the rotational progression including even and odd levels. The lower spectrum shows the effect of atom spin polarization. A weak auxiliary laser beam (5 mW cm^{-2}), circularly polarized and tuned to the $3\,^2S_{1/2}(f=2)\rightarrow 3\,^2P_{3/2}(f=3)$ transition, crosses the atom beam at right angles 2 cm upstream from the PA laser. This auxiliary laser optically pumps population to the $3\,^2S_{1/2}(f=2,M_f=2)$ ground state. The photoassociation collision then involves two identical bosons, and all odd partial waves are

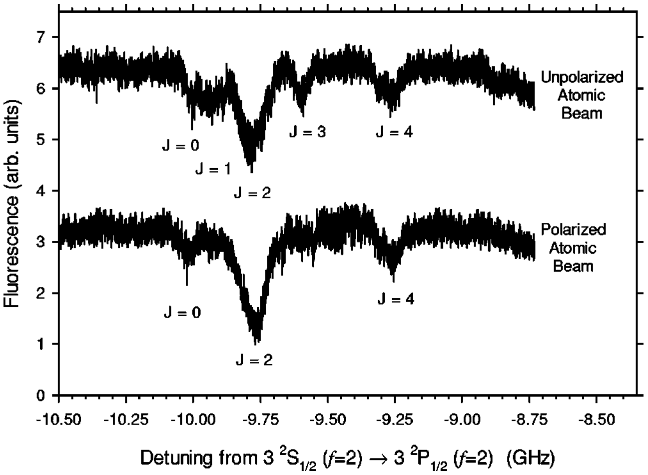

FIG. 5. Beam-loss spectra for parallel PA light polarization close to the dip occurring at $\simeq -10$ GHz detuning to the red of the $^2S_{1/2}(f=2)+{}^2P_{1/2}(f=2)$ dissociation limit.

excluded from the photoassociation collision. The odd rotational levels are missing from the lower spectrum of Fig. 5. A similar effect was observed in the photoassociative ionization spectrum of ^{85}Rb atoms in an optical dipole trap [12].

B. Extraction of rotational constants

Conventional spectroscopy theory predicts the rotational energy of a diatomic molecule (nonrigid rotator), measured from the rotational level having $J=0$, to be [13]

$$F(J) = B_v J(J+1) - D_v J^2(J+1)^2, \tag{1}$$

where J is the rotational quantum number and B_v is the rotational constant. The value of D_v that represents the effects of the centrifugal force is much smaller than B_v and we omit it. We use the first term on the right-hand side of Eq. (1) to extract the rotational constant between different levels, using the experimental values from Fig. 5. Table II lists the measured energy values together with the computed values for B_v. The computed value for B_v is close to the weak-field value predicted for the 0_g^- molecular potential of 37.8 MHz [14]. That this rotational progression is not more severely broadened and shifted is surprising in view of the high intensity of the photoassociation field.

TABLE II. Measured values of ΔF and calculated values for the rotational constant B_v. The experimental data are taken from the spectra in Fig. 5. The data in the first three rows come from the polarized beam spectrum, while the data in the last three rows come from the unpolarized spectrum.

	$\Delta F = F(J') - F(J'')$ (GHz)	B_v (MHz)
$J'=0 \rightarrow J''=2$	$0.25 \pm 0.02 = 6B_v$	41.7 ± 3.2
$J'=0 \rightarrow J''=4$	$0.76 \pm 0.02 = 20B_v$	38.0 ± 1.0
$J'=2 \rightarrow J''=4$	$0.51 \pm 0.03 = 14B_v$	36.4 ± 2.2
$J'=2 \rightarrow J''=3$	$0.185 \pm 0.03 = 6B_v$	30.8 ± 5.0
$J'=2 \rightarrow J''=4$	$0.51 \pm 0.03 = 14B_v$	36.4 ± 2.2
$J'=3 \rightarrow J''=4$	$0.325 \pm 0.02 = 8B_v$	40.6 ± 2.5

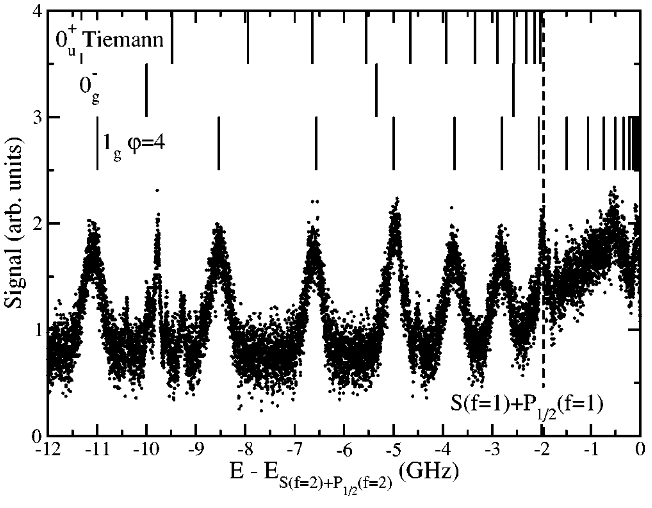

FIG. 6. Assignment of the beam-loss spectrum. The spectrum exhibits a series of features that appear to cut off at the $^2S(f=1)+{}^2P_{1/2}(f=1)$ hyperfine limit, as indicated by the vertical dashed line. The zero of detuning is the $^2S(f=2)+{}^2P_{1/2}(f=2)$ hyperfine limit. Each feature of this progression is about 0.5 GHz wide. In addition, between −10 GHz and −9 GHz there is a sharper feature which is associated with a rotational progression, as already pointed out in Secs. III A and III B. The spectrum labeled "0_u^+ Tiemann" refers to the determination of Ref. [19]; the label "0_g^-" refers to the vibrational progression calculated from the adiabatic Movre-Pichler potential [16]. The progression labeled by "$1_g \varphi=4$" refers to the 1_g adiabatic Movre-Pichler potential with $\varphi = \Omega + \iota$, as explained in the text.

Our beam-loss spectrum can be compared to the photoassociative spectra that have been observed for Na atoms trapped in a dark spot MOT at much lower temperatures near 0.5 mK [9] (see the inset in Fig. 8). Features in the MOT spectrum due to the $A\,^1\Sigma_u^+(0_u^+)$ state do not appear in the beam-loss spectrum. The 0_g^- and 1_g features measured in weak-field MOT are shifted by about 1 GHz to the red in the strong-field beam-loss spectrum. Even taking into account this shift, feature details do not match exactly. The differences are due to shifts and power broadening induced by strong-field effects. In Sec. III C we present an approximate analysis based on the strong-field theories in Refs. [11,15]. We identify the progressions with specific excited-state potentials and propose an explanation for the survival of these high-resolution spectra even in a strong-field environment.

C. Interpretation of the spectra

1. Molecular potentials and spectral assignments

Figure 6 repeats the beam-loss photoassociation spectrum (here inverted) as a function of detuning from the $^2S(f=2)+{}^2P_{1/2}(f=2)$ dissociation limit. The spectrum exhibits a clear vibrational progression that cuts off at the $^2S(f=1)+{}^2P_{1/2}(f=1)$ hyperfine limit, having features about 0.5 GHz wide. In addition, between −10 GHz and −9 GHz we note the rotational progression, having features about 100 MHz wide, as-

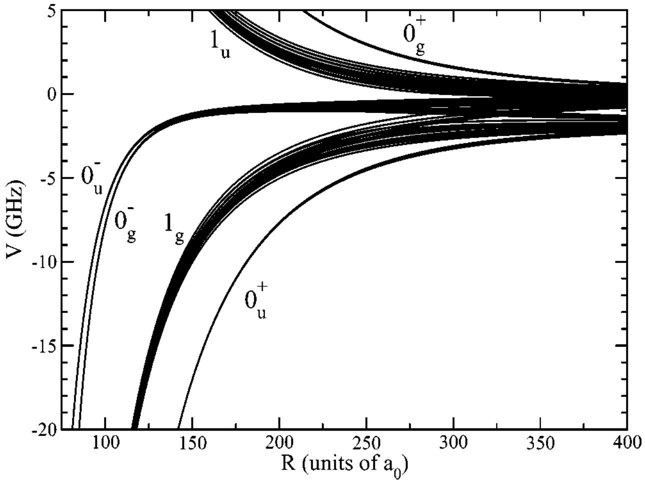

FIG. 7. Hyperfine adiabatic potentials near the $^2S+^2P_{1/2}$ fine-structure limit as a function of internuclear separation, where $1a_0=0.0529$ nm. The labeled states correlate to the $^2S+^2P_{1/2}$ fine structure limit and the $0_g^-, 1_g$, and 0_u^+ states are optically coupled to the ground state.

sociated with a single vibrational level, and discussed in Sec. III A and III B. The markers above the experimental spectrum indicate our assignments that are based primarily on a Hund's case (c) coupling scheme and adiabatic Movre-Pichler potentials [16]. These potentials are labeled by $\Omega_\sigma^\pm$, where Ω is the absolute value of the projection of the total electronic angular momentum along the internuclear axis and σ is gerade or ungerade for inversion symmetry of the electronic wave function around the center of charge. For $\Omega=0$ levels the ± superscript labels the reflection symmetry of the electronic wave function through a plane containing the internuclear axis.

Figure 7 indicates how the adiabatic hyperfine potentials correlate for $R\leqslant 400a_0$ with six adiabatic Movre-Pichler potentials dissociating to the $^2S+^2P_{1/2}$ fine-structure limit. Three of these, labeled 0_u^+, 0_g^-, and 1_g, are optically coupled to the ground state. At short internuclear separation, where the molecular binding energy is large compared to the atomic fine-structure splitting of the ^2P atom, the 0_u^+ correlates to the $A\,^1\Sigma_u^+$ potential and both 0_g^- and 1_g correlate to the $1\,^3\Sigma_g^+$ potential. However, the Movre-Pichler model does not take into account the hyperfine structure of the Na atoms. In our spectrum we observe levels with binding energies on the order of the ^2S and ^2P hyperfine splitting. Adiabatic potentials that include molecular binding, atomic fine structure, and hyperfine structure, are labeled by $\varphi=\Omega+\iota$, where ι is the projection of the total nuclear spin along the internuclear axis. All hyperfine adiabats near the $^2S+^2P_{1/2}$ fine-structure limit are shown in Fig. 7. The atomic fine- and hyperfine-structure splittings and long-range dipolar interaction coefficients of Ref. [17] have been used. The hyperfine interaction leads to small splittings for $\Omega=0$ symmetries. For example, the 0_g^- feature near -10 GHz has rotational splittings that are larger than the hyperfine splittings. For $\Omega=1$ the hyperfine interactions induce noticeable splittings. Following Ref. [18] the hyperfine splitting is proportional to $\Omega\iota$ and, near the hyperfine dissociation limits, is larger than the nuclear rotational energies. The hyperfine adiabat corresponding to the Movre-Pichler 1_g adiabat with maximal $\varphi,\iota=4,3$ is, to good approximation, given by the Movre-Pichler adiabat shifted to dissociate to the $^2S(f=2)+^2P_{1/2}(f=2)$ hyperfine limit.

The rotational and vibrational energy structure of the 0_u^+ state has been observed in Ref. [19]. The "stick spectrum" corresponding to this data is shown in Fig. 6. It is clear from Fig. 6, however, that the beam-loss spectra do not correspond to the 0_u^+ state. The measured spectra have wider vibrational spacings most consistent with a shorter-range 1_g potential. We explain below that the absence of 0_u^+ features are a consequence of strong power broadening of these features.

The $1\,^3\Sigma_g^+$ potential (to which the 0_g^- and 1_g states correlate) is fairly well known at short internuclear separations [20]. Long-range spectroscopic data on the $\Omega=0$ and $\Omega=1$ fine-structure components of the $1\,^3\Sigma_g^+$ potential, however, are limited [21]. Consequently, we have modified the short-range shape of the $1\,^3\Sigma_g^+$ potential such that a vibrational level of the $\varphi=4$ 1_g hyperfine adiabat matches the peak of the measured feature at -11 GHz. All other 1_g vibrational levels below the $^2S(f=1)+^2P_{1/2}(f=1)$ hyperfine limit are then determined and coincide with the measured features. Other φ 1_g adiabats could not be made to agree with the observed vibrational spacings. The $\varphi=0$ 1_g adiabat, for example, dissociates to the $^2S(f=1)+^2P_{1/2}(f=1)$ hyperfine limit and, consequently, has a narrower vibrational spacing than the observed spectrum. The spectrum of the $\varphi=4$ 1_g vibrational levels above the $^2S(f=1)+^2P_{1/2}(f=1)$ hyperfine limit is presumably obscured due to predissociation. The 0_g^- Movre-Pichler adiabat has three vibrational levels between -12 GHz and -2 GHz below the $^2S(f=2)+^2P_{1/2}(f=2)$ hyperfine limit. Only one of these levels has been clearly observed in our experiment. The other two are likely hidden by the 1_g features.

The narrow feature around -9.5 GHz in Fig. 6 is shown expanded in Figs. 4 and 5 and again (inverted) for convenience in Fig. 8. We assign this feature a 0_g^- vibrational level. A clear rotational series is observed with a rotational constant $B_v\simeq 38$ MHz that agrees with the rotational constant obtained from the 0_g^- adiabat. Each rotational level, as shown in Fig. 8, is labeled by J, the total angular momentum of the molecule without nuclear spin. Note that high J lines are only accessible from high collisional partial waves l between $^2S(f=2)$ atoms. In fact for the 0_g^- state near the $^2S+^2P_{1/2}$ limit $J\approx l$, with small contributions from $J=l\pm 2$ as discussed in Ref. [22].

2. Theoretical line profiles

Because of the high laser power and one-dimensional beam geometry in these experiments, it is necessary to make some modifications to the standard weak-field photoassociation line shapes [23–25] in order to model these spectra. We adapt the strong-field theory of Refs. [11,15] for the photoassociation rate constant $K(T,\omega)$ at temperature T and frequency ω to provide a framework for discussing the line profiles. Figure 8 compares experimental data with line shapes of the 0_g^- rotational progression calculated as described below. The thermally averaged profile is

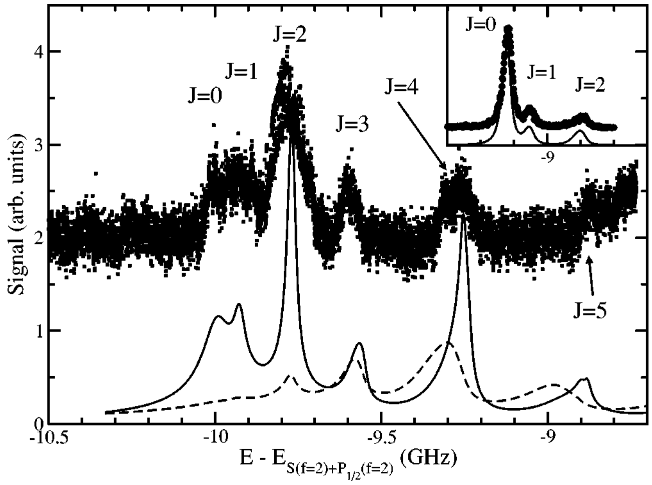

FIG. 8. Comparison of the measured rotational progression of the 0_g^- vibrational line near −10 GHz shown in Fig. 6 to two calculated line shapes. The solid-line spectrum is obtained using the one-dimensional beam velocity distribution at $T=4$ mK. The dotted-line spectrum assumes a thermal gas cell experiment at $T=4$ mK. The inset compares the weak-field PAI spectrum (points) measured in a dark spot MOT at a collision temperature of $T=4$ mK [9] with the calculated MOT spectrum (solid line) using Eqs. (2) and (3) with the isotropic gas velocity distribution function. The horizontal scale is the same for the inset as for the figure. Only *s*, *p*, and *d* waves contribute to the MOT spectrum because of the colder MOT temperature. Note that the beam spectrum is shifted ≃−1 GHz relative to the MOT spectrum.

$$K(T,\omega) = \int_0^\infty f(E,T)K(E,\omega)dE, \tag{2}$$

where $f(E,T)$ is the distribution function for atoms with relative collision energy E. For a single excited rovibrational hyperfine level b

$$K_{bi}(E_i,\omega) = \frac{\pi v_i}{k_i^2}\,\frac{\gamma_b\Gamma_{bi}(E_i)}{[E_i+\hbar\omega-E_b-S_b(E_i)]^2+[\gamma_b+\Gamma_{bi}^{tot}(E_i)]^2/4}, \tag{3}$$

where v_i is the relative velocity and $k_i=\sqrt{2\mu E_i/\hbar^2}$ the corresponding wave number for the reduced mass μ. E_b and γ_b are the energy and natural linewidth of excited level b and $S_b(E_i)$ is an energy shift due to the light-induced coupling; $\Gamma_{bi}(E_i)$ is the stimulated emission width from the excited bound level b to the ground-state scattering channel i. Both S_b and Γ_{bi} are proportional to laser intensity. The *total* stimulated emission width from level b to the ground-state scattering channels at collision kinetic energy E_i is

$$\Gamma_{bi}^{tot}(E_i) = \Gamma_{bi}(E_i) + \sum_{j\neq i}\Gamma_{bj}(E_j) = \Gamma_{bi}(E_i) + \Gamma_{bi}^{o}. \tag{4}$$

Here we have separated off the ground entrance channel i from other ground-state channels $j\neq i$. The other channels contribute Γ_{bi}^{o} to the total width Γ_{bi}^{tot}. The channel is specified by giving the quantum numbers of the separated atoms and the relative angular-momentum (or partial wave) quantum number.

The photoassociation rate used in Eq. (3) is the same as that in Eq. (3.11) of Ref. [11], except that it includes broadening to multiple ground-state channels. Expressions similar to Eq. (3) have appeared elsewhere in the literature; the stimulated emission width $\Gamma_{bi}(E)$ is defined as $\gamma_s(\varepsilon,l)$ in Eq. (3) of Ref. [23] and by the matrix element expression in Eq. (1) of Ref. [25]. The stimulated emission widths represent the Fermi golden rule decay rates of the bound state b into the ground-state channels j with asymptotic kinetic energy E_j and partial wave l:

$$\Gamma_{bj} = 2\pi|\langle b|\vec{\mathcal{E}}\cdot\vec{d}|E_{bj},l\rangle|^2, \tag{5}$$

where $\vec{\mathcal{E}}$ is the electric field of the laser and $\vec{d}$ is the molecular transition dipole moment operator. When $j=i$ represents the entrance channel, the quantum threshold laws ensure that $\Gamma_{bi}\propto E_i^{l+1/2}$ vanishes as collision kinetic energy $E_i\rightarrow 0$ in the entrance channel. This law applies in our case for T below about 1 mK. The d- and g-partial-wave centrifugal barriers are at collision energies of 5 mK and 30 mK, respectively.

The emission rates to other ground-state channels, $\Gamma_{bj}(E_j)$, $j\neq i$, will not vanish unless they are threshold channels. Consequently, $\Gamma_{bi}^{tot}(E)\geqslant\Gamma_{bi}(E)$. If j represents a $^2S(f=1)+{}^2S(f=2)$ or $^2S(f=1)+{}^2S(f=1)$ channel, then E_j is $E_{\mathrm{hf}}+E_i$ and $2E_{\mathrm{hf}}+E_i$, respectively. Here E_{hf} is the hyperfine splitting between the $f=1$ and $f=2$ level. Since $E_{\mathrm{hf}}\gg k_BT$ the collision-energy dependence of $\Gamma_{bj}(E_j)$ for these nonthreshold channels is negligible.

Since the transverse temperature in the beam is an order of magnitude lower than the $T=4$ mK longitudinal temperature, the collisions are "quasi-one-dimensional" along the atom beam axis. This beam geometry is taken into account by using the one-dimensional distribution function [26]

$$f_{1D}(E,T) = \frac{1}{\sqrt{\pi}}\frac{e^{-x}}{\sqrt{x}}, \tag{6}$$

where $x=E/k_BT$. This assumes no energy variation in the two directions transverse to the atom beam. This contrasts to the usual three dimensional distribution function for an isotropic gas

$$f_{3\mathrm{D}}(E,T) = \frac{2}{\sqrt{\pi}}\sqrt{x}e^{-x}. \tag{7}$$

The $1/\sqrt{x}$ factor for the bright-beam collisions results in lower collision energies having greater weight.

At low laser intensities, photoassociation line shapes calculated according to Eq. (3) are generally found to be in good agreement with observations [11,23–25,27,28], even at modest laser intensities. Equation (3) shows two effects of increasing the laser intensity. Since the width $\Gamma_i(E)$ and shift $S_b(E)$ are proportional to laser power, photoassociation lines show intensity-dependent line shifts [11,28–30] and power broadening [11,31]. The latter occurs when $\Gamma_i(E)$ becomes on the order of or larger than γ_b. The width can be calculated directly from the ground- and excited-state wave functions.

Shifts are more complicated to calculate, requiring either the ground-state Green's function [11] or a configuration-interaction sum [15]. The reflection approximation (Eqs. (3.6) and (3.7) of Ref. [11]) can be used to estimate the magnitude of $\Gamma_{bi}(E)$ and $S_b(E)$ for our case. At the experimental laser intensity for the transition from two colliding $^2S(f=2)$ atoms to a vibrational level a few gigahertz below the atomic hyperfine limits, $\Gamma_{bi}(E)$ is orders of magnitude larger than γ_b for most collisional partial waves and collision energies E typical of a MOT or the bright beam. The shifts tend also to be large, even larger than the spacing between levels. Since the effect of the high-intensity light is so large, it may be questioned whether the formula (3) is applicable in this case. However, the ability to account for a number of experimental features makes our approach useful in the absence of a theory that fully accounts for the strong-field dressing of the colliding atoms. Since we are able to calculate the width terms from the known molecular physics of the ground and excited states of the Na_2 dimer, and given the unknown reliability of the reflection approximation for calculating shifts associated with large Condon points, we will use calculated widths in Eq. (3) but will introduce the shifts phenomenologically by adjusting the short-range part of a given molecular potential to cause a shift that brings the calculated line into agreement with the measured one for the experimental case, as discussed in the Sec. III B for the 1_g series. This represents a phenomenological way to introduce the effect of field-dressed potentials.

Figure 8 shows calculated and observed line profiles for the 0_g^- feature near −10 GHz. The calculation of the width was carried out as in Ref. [25], using the full hyperfine structure in the ground and excited states and the known ground- and excited-state potentials [32], and summing over the contributing hyperfine substructure. Our calculated profile for the photoassociation spectrum in a 500 μK MOT with the three-dimensional distribution, Eq. (7), is compared to NIST data [9] in the inset of Fig. 8. The excellent agreement between theory and experiment for the three $J=0$, 1, and 2 lines is evident for this weak-field case. The figure also shows our strong-field calculation, assuming $I=600\ \mathrm{W/cm^2}$, equal population of all $f=2$ magnetic sublevels, and $\Gamma_{bi}^{tot}(E) \simeq \Gamma_{bi}(E)$. The calculated $J=0$ peak was shifted by −0.9 GHz from the weak-field MOT peak. The calculated profile using the one-dimensional energy distribution, Eq. (6), for $T=4$ mK is in remarkable qualitative agreement with the experimental profile. Linewidths are fairly well reproduced. The relatively narrow lines result from collision energies E for which $\Gamma_{bi}(E)$ is small; collision energies for which $\Gamma_{bi}(E)$ is large only contribute to a broad power-broadened background. A simulation with an additional energy-independent broadening of 20 MHz–50 MHz [i.e., $\Gamma_{bi}^{tot}(E)=\Gamma_{bi}(E)+20\text{–}50$ MHz] to incorporate losses to $^2S(f\text{-}1)+{}^2S(f=2)$ and $^2S(f\text{-}1)+{}^2S(f=1)$ collision channels leads to an even better fit. Figure 8 also shows the calculated profile using the three dimensional distribution function, Eq. (7), for a gas cell at $T=4$ mk for $I=600\ \mathrm{W/cm^2}$. The markedly different profile has the $J=4$ feature as the strongest one, while the $J<3$ lines are nearly absent. In addition the rotational lines are significantly broader. Due to the $1/\sqrt{E}$ factor in Eq. (6), line shapes from the quasi-one-dimensional collisions in our beam favor contributions from lower collision energies. This ensures that small J features are stronger than for higher J and that the lines are narrower since Wigner threshold effects reduce $\Gamma_{bi}(E)$ at colder collision energies [15].

For the results presented in Fig. 8 we could only calculate $\Gamma_{bi}(E)$ for two colliding $^2S(f=2)$ atoms. The two-photon measurements and calculations on vibrational levels of the $A^1\Sigma_u^+$ potential [32] (to which the 0_u^+ correlates) and the calculations for the $1\,^3\Sigma_g^+$ potential tens of cm^{-1} below the $^2S+{}^2P_{1/2}$ dissociation limit have been used to estimate the relative size of the transition strengths to the three $^2S+{}^2S$ hyperfine limits from the $1\,^3\Sigma_g^+$ and $A^1\Sigma_u^+$ states. For the $1\,^3\Sigma_g^+$ state $\Gamma_{bi}^{tot}(E)\simeq\Gamma_{bi}(E)$ while for the $A\,^1\Sigma_u^+$ state $\Gamma_{bi}^{tot}(E)\gg\Gamma_{bi}(E)$. This means that most of the transition strength coupling to the $1\,^3\Sigma_g^+(0_g^-,1_g)$ state is associated with two colliding $^2S(f=2)$ atoms, while most of the transition strength coupling to the $A\,^1\Sigma_g^+(0_u^+)$ state is associated with colliding partners including at least one $^2S(f=1)$ atom. Line shapes of the rovibrational levels of the $A\,^1\Sigma_u^+$ potential show that when $\Gamma_{bi}^{tot}(E)\gg\Gamma_{bi}(E)$ the lines exhibit broadening to hundreds of times the natural linewidth. As a consequence we would expect that spectral structure associated with the 0_u^+ state would be power broadened into the background under the conditions of our experiment, and it is therefore not surprising that Fig. 6 exhibits no distinct 0_u^+ features.

We calculated the line shape of the 1_g vibrational levels under the same conditions and found features with a width ≈1 GHz. This theoretical width is consistent with overlapping lines from the hyperfine structure of a 1_g vibrational level [18] and is consistent with the observed spread of about 1 GHz in the NIST 1_g MOT spectrum [9]. The MOT 1_g feature centered near −10 GHz is also shifted about 1 GHz with respect to neighboring 1_g features in the beam spectrum. The 1_g features of the beam experiment have a narrower width ≈0.5 GHz. This suggests that the linearly polarized PA laser may not excite all the 1_g hyperfine states. Since the observed progression is consistent with the vibrational series of the $\varphi=4$ 1_g adiabatic potentials and not with other φ, we speculate that the atom beam preparation (transverse cooling, passage through the 2D MOT, etc.) might have induced a partial atomic polarization alignment resulting in the predominance of $\varphi=4$ collisions along the internuclear axis. Linear polarization along the atom beam axis favors transitions to larger φ.

We note finally some reservations concerning the comparison of the observed and calculated line profiles. Clearly, a proper high-intensity theory is still to be formulated. Our treatment of the large light shifts for lines so near the separated atom limit is only phenomenological. The intense light can induce coupling between several excited-state levels and several ground-state partial waves. Finally the preparation of the atomic beam before the photoassociation step might introduce an uncontrolled atomic polarization. None of these effects is included and consequently our model should only be considered as semiquantitative.

IV. SUMMARY AND CONCLUSIONS

Features of the beam-loss spectra originating from quasi-one-dimensional photoassociation collisions in a bright sodium atom beam have been identified with vibrational progressions of the 1_g and 0_g^- hyperfine adiabatic potentials dissociating to the $^2S+^2P_{1/2}$ limit. Furthermore, line shapes of the first few members of a rotational progression associated with one of the 0_g^- vibrational levels have been analyzed in terms of a line profile model, taking into account the energy distribution characteristic of one-dimensional collisions and power broadening due to the high intensity of the PA laser. It is found, by comparing calculated spectra from one- and three-dimensional collision environments at the same PA laser intensity, that the one-dimensional thermal averaging tends to favor lower-energy collisions which in turn markedly reduces power broadening of spectral features and increases population of lower rotational levels. It is estimated that optical coupling from colliding ground-state atoms to the 0_u^+ potential will be much greater than for either of the $0_g^-, 1_g$ states individually and effectively power broaden 0_u^+ spectral features into the background. Finally the observed linewidths of the 1_g vibrational progression are about a factor of 2 narrower than those expected from calculations including the entire 1_g molecular hyperfine manifold. It is suggested that in the experiment colliding atoms may be partially polarized, effectively excluding a subset of the molecular hyperfine manifold.

[1] P. L. Gould, P. D. Lett, P. S. Julienne, W. D. Phillips, H. R. Thorsheim, and J. Weiner, Phys. Rev. Lett. **60**, 788 (1988).

[2] For a review of cold and ultracold collisions, see J. Weiner, V. S. Bagnato, S. Zilio, and P. S. Julienne, Rev. Mod. Phys. **71**, 1 (1999).

[3] W. C. Stwalley, and H. Wang, J. Mol. Spectrosc. **195**, 194 (1999).

[4] K. M. Jones, S. Maleki, L. P. Ratliff, and P. D. Lett, J. Phys. B **30**, 289 (1997).

[5] P. D. Lett, P. S. Julienne, and W. D. Phillips, Annu. Rev. Phys. Chem. **46**, 423 (1995).

[6] W. DeGraffenreid, J. Ramirez-Serrano, Y-M Liu, A. Rosenbaum, and J. Weiner, Appl. Phys. B: Lasers Opt. **B71**, 881 (2000).

[7] J. Ramirez-Serrano, W. DeGraffenreid, and J. Weiner, Phys. Rev. A **65**, 052719 (2002).

[8] W. DeGraffenreid, J. Ramirez-Serrano, Y-M. Liu, and J. Weiner, Rev. Sci. Instrum. **71**, 3668 (2000).

[9] F. Fatemi, K. Jones, and P. D. Lett (unpublished).

[10] P. S. Julienne, J. Res. Natl. Inst. Stand. Technol. **101**, 487 (1996).

[11] J. L. Bohn and P. S. Julienne, Phys. Rev. A **60**, 414 (1999).

[12] J. R. Gardner, R. A. Cline, J. D. Miller, D. J. Heinzen, H. M. J. M. Boesten, and B. J. Verhaar, Phys. Rev. Lett. **74**, 3764 (1995).

[13] G. Herzberg, *Molecular Spectra and Molecular Structure. I. Spectra of Diatomic Molecules* (Van Nostrand, Princeton, NJ, 1950).

[14] E. Tiesinga and P. S. Julienne (unpublished).

[15] A. Simoni, P. S. Julienne, E. Tiesinga, and C. J. Williams, Phys. Rev. A **66**, 063406 (2002).

[16] M. Movre and G. Pichler, J. Phys. B **10**, 2631 (1977).

[17] K. M. Jones, P. S. Julienne, P. D. Lett, W. D. Phillips, E. Tiesinga, and C. J. Williams, Europhys. Lett. **35**, 85 (1996).

[18] X. Wang, H. Wang, P. L. Gould, W. C. Stwalley, E. Tiesinga, and P. S. Julienne, Phys. Rev. A **57**, 4600 (1998).

[19] M. Elbs, O. Keck, H. Knöckel, and E. Tiemann, Z. Phys. D: At., Mol. Clusters **42**, 49 (1997).

[20] A. Fäbert, J. Koch, T. Platz, and W. Demtröder, Chem. Phys. Lett. **223**, 546 (1994).

[21] L. E. E. de Araujo, J. D. Weinstein, S. D. Gensemer, F. K. Fatemi, K. M. Jones, P. D. Lett, and E. Tiesinga, J. Chem. Phys. **119**, 2062 (2003).

[22] J. R. Gardner, R. A. Cline, J. D. Miller, D. J. Heinzen, H.M.J.M. Boesten, and B.J. Verhaar, Phys. Rev. Lett. **74**, 3764 (1995).

[23] R. Napolitano, J. Weiner, C. J. Williams, and P. S. Julienne, Phys. Rev. Lett. **73**, 1352 (1994).

[24] K. Jones, P. D. Lett, E. Tiesinga, and P. S. Julienne, Phys. Rev. A **61**, 012501 (1999).

[25] E. Tiesinga, C. J. Williams, P. S. Julienne, K. M. Jones, P. D. Lett, and W. D. Phillips, J. Res. Natl. Inst. Stand. Technol. **101**, 505 (1996).

[26] J. Ramirez-Serrano, Ph.D. thesis, University of Maryland, 2001 (unpublished).

[27] J. P. Burke, C. H. Greene, J. L. Bohn, H. Wang, P. L. Gould, and W. C. Stwalley, Phys. Rev. A **60**, 4417 (1999).

[28] C. McKenzie, J. H. Denschlag, H. Häffner, A. Browaeys, L. E. E. de Araujo, F. K. Fatemi, K. M. Jones, J. E. Simsarian, D. Cho, A. Simoni, E. Tiesinga, P. S. Julienne, K. Helmerson, P. D. Lett, S. L. Rolston, and W. D. Phillips, Phys. Rev. Lett. **88**, 120403 (2002).

[29] P. O. Fedichev, Y. Kagan, G. V. Shlyapnikov, and J. T.M. Walraven, Phys. Rev. Lett. **77**, 2913 (1996).

[30] J. M. Gerton, B. J. Frew, and R. G. Hulet, Phys. Rev. A **64**, 053410 (2001).

[31] I. D. Prodan, M. Pichler, M. Junker, R. G. Hulet, and J. Bohn, Phys. Rev. Lett. **91**, 080402 (2003).

[32] C. Samuelis, E. Tiesinga, T. Laue, M. Elbs, H. Knöckel, and E. Tiemann, Phys. Rev. A **63**, 012710 (2000).